


 Cite this: *RSC Adv.*, 2024, 14, 3909

Interpretable machine learning-assisted screening of perovskite oxides†

 Jie Zhao,^{id}*^a Xiaoyan Wang,^{id}*^b Haobo Li^c and Xiaoyong Xu^{id}*^c

Perovskite oxides are extensively utilized in energy storage and conversion. However, they are conventionally screened *via* time-consuming and cost-intensive experimental approaches and density functional theory. Herein, interpretable machine learning is applied to identify perovskite oxides from virtual perovskite-type combinations by constructing classification and regression models to predict their thermodynamic stability and energy above the convex hull (E_h), respectively, and interpreting the models using SHapley Additive exPlanations. The highest occupied molecular orbital energy and the elastic modulus of the B-site elements of perovskite oxides are the top two features for stability prediction, whereas the Stability Label and features involving the elastic modulus and ionic radius are crucial for E_h regression. A classification model, which displays an accuracy of 0.919, precision of 0.937, F1-score of 0.932, and recall of 0.935, screens 682 143 stable perovskite oxides from 1 126 668 virtual perovskite-type combinations. The E_h values of the predicted stable perovskites are forecasted by a regression model with a coefficient of determination of 0.916, and root mean square error of 24.2 meV atom⁻¹. Good agreement is observed between the regression model predicted and density functional theory-calculated E_h values.

Received 15th December 2023

Accepted 21st January 2024

DOI: 10.1039/d3ra08591k

rsc.li/rsc-advances

1. Introduction

Perovskite oxides have attracted significant attention as prospective materials for a diverse range of scientific applications due to their fascinating physical and chemical properties.^{1,2} Notably, perovskite oxides that manifest both ionic and electronic conductivities and possess catalytic activities for oxygen reduction and fuel oxidation are frequently employed as electrode materials in solid oxide fuel cells.^{3–5} Additionally, they also have been broadly utilized as chemical sensors, photocatalysts for water splitting, and electrode materials for batteries and supercapacitors.^{6–8}

The wide-ranging applications of perovskite oxides can also be attributed to their compositional flexibility.⁹ The structure diagrams of single and double perovskite oxides are displayed in Fig. 1. Despite the simple general formula of single perovskite oxides for ABO₃ and double perovskite oxides for A₂B'B''O₆, where A and B are different metal cations, and O represents oxygen, a wide variety of cations can be incorporated into their A- and B-sites.¹⁰ For an ideal cubic perovskite oxide, the larger A-

site cation, typically a rare-earth or alkaline-earth metal, is situated in a 12-fold coordinated site surrounded by 12 oxygen ions. In comparison, the smaller B-site cation, usually a transition metal, occupies an octahedral site surrounded by six oxygen ions (BO₆ octahedron).²

Up to now, several strategies have been proposed to screen thermodynamically stable perovskite oxides from perovskite-type compounds. Among these approaches, empirical regularities are initially advocated. For example, Goldschmidt suggested a tolerance factor, defined as

$$t = \frac{(r_A + r_O)}{\sqrt{2}(r_B + r_O)} \quad (1)$$

where r_A , r_B , and r_O are the ionic radii of A, B, and O, respectively.¹² For cubic perovskite oxides, t is close to 1. Perovskite oxides with t in the range of 0.76 to 1.13 were extensively observed.² However, the accuracy of t in distinguishing

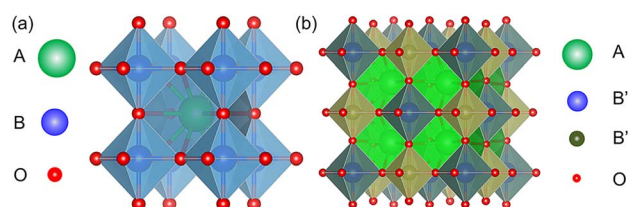


Fig. 1 Structure diagrams of (a) single and (b) double perovskite oxides.¹¹

^aCollege of Chemical Engineering, Nanjing Tech University, Nanjing, Jiangsu 211816, China. E-mail: j.zhao1@njtech.edu.cn

^bSchool of Computer Science, Nanjing Audit University, Nanjing, Jiangsu 211815, China. E-mail: xywang@nau.edu.cn

^cSchool of Chemical Engineering, The University of Adelaide, Adelaide, SA 5005, Australia. E-mail: xiaoyong.xu@adelaide.edu.au

† Electronic supplementary information (ESI) available. See DOI: <https://doi.org/10.1039/d3ra08591k>



perovskites and non-perovskites is only 83%.¹⁰ Bartel *et al.*¹⁰ proposed a new tolerance factor

$$\tau = \frac{r_{\text{O}}}{r_{\text{B}}} - n_{\text{A}} \left(n_{\text{A}} - \frac{r_{\text{A}}/r_{\text{B}}}{\ln(r_{\text{A}}/r_{\text{B}})} \right) \quad (2)$$

where n_{A} is the oxidation state of A, and r_{A} , r_{B} , and r_{O} are the ionic radii of A, B, and O, respectively. It was found that $\tau < 4.18$ reveals perovskite oxides with an accuracy of 92%. Feng *et al.*¹³ proposed an octahedral factor μ ($\mu = r_{\text{B}}/r_{\text{O}}$), which displayed comparable importance with t in predicting the stability of cubic perovskite oxides. The octahedral factor for cubic perovskites is in the range of 0.414 to 0.732. Zhang *et al.*¹⁴ recommended a bond-valence calculated tolerance factor (t_{BV}) to screen stable perovskite oxides. They observed that the t_{BV} for perovskite oxides lies in the range of 0.822–1.139. Song and Yin¹⁵ utilized a descriptor $(\mu + t)\eta$ to indicate the stability of perovskites with an accuracy of $\sim 90\%$, where μ , t , and η are the octahedral factor, Goldschmidt tolerance factor, and atomic packing fraction, respectively. η is calculated using the equation $\eta = (V_{\text{A}} + V_{\text{B}} + 3V_{\text{X}})/a^3$, where V_{A} , V_{B} , V_{X} , and a represent the atomic volumes of A, B, and X for ABX_3 perovskites and the lattice constant of the cubic cells, respectively.

Density functional theory (DFT) was also employed to predict the thermodynamic stability of perovskite oxides. This is achieved by the calculation of their energy above the convex hull (E_{h}).^{16–20} Basically, E_{h} is calculated with the energy difference between the perovskite oxides and the convex hull which is constructed by linking phases or linear combination of phases with the lowest formation energy using tie lines at specific compositions.^{17,21} It can be calculated by eqn (3) and (4):¹⁷

$$H_{\text{f}}^{\text{ABO}_3} = E(\text{ABO}_3) - \mu_{\text{A}} - \mu_{\text{B}} - 3\mu_{\text{O}} \quad (3)$$

$$E_{\text{h}}^{\text{ABO}_3} = H_{\text{f}}^{\text{ABO}_3} - H_{\text{f}} \quad (4)$$

where $H_{\text{f}}^{\text{ABO}_3}$ and $E(\text{ABO}_3)$ are the formation energy and total energy of the ABO_3 compound, respectively, μ_{A} , μ_{B} and μ_{O} are the chemical potentials of A, B and O, respectively, and $E_{\text{h}}^{\text{ABO}_3}$ and H_{f} are the energy above the convex hull and the convex hull energy of the ABO_3 compound, respectively.

Theoretically, for stable perovskite oxides, their E_{h} values equal to zero. The bigger the E_{h} values, the worse the phase stability of perovskite oxides.²² For instance, Emery *et al.*¹⁸ filtered 383 perovskite oxides for thermochemical water splitting from 5329 ABO_3 compounds based on the criteria of their stability and oxygen vacancy formation energy using high-throughput DFT. Jacobs *et al.*¹⁹ used high-throughput DFT to investigate the phase stability of perovskite oxides under their operating conditions. They calculated the E_{h} values of 2145 perovskite compounds and obtained 52 potential perovskite cathode materials for solid oxide fuel cells with superior thermodynamic stability. Ma *et al.*²³ employed DFT calculations to screen stable perovskite oxides for high-power vacuum electronic and thermionic energy conversion devices. From 2900 perovskite oxides, they obtained seven promising candidates with the E_{h} values of lower than 42 meV atom⁻¹. Emery and Wolverton¹⁷ predicted the thermodynamic stability of 5329 compounds using DFT, from which 395 stable

perovskite oxides were filtered based on the E_{h} threshold value of 25 meV atom⁻¹.

Even though DFT is effective in predicting the stability of perovskite oxides, it is limited by high cost and computation time.^{24,25} Recently, machine learning (ML) methods have been employed to predict the stability and/or E_{h} values of perovskite oxides.^{22,26–31} ML models are constructed on sample data originating from experimental and computational methods to make classification and regression with higher efficiency, lower cost, and less computation time.²⁵ For example, Zhao and Wang¹² built a random forest classification model to predict the stability of single perovskite oxides. They found that the highest occupied molecular orbital (HOMO) energy and Zunger's pseudopotential radius of the B-site elements were two of the most important features. 430 stable perovskite oxides such as HfVO_3 , OsVO_3 , and TaCrO_3 were screened from 2229 perovskite-type combinations under the threshold of $E_{\text{h}} \leq 50$ meV atom⁻¹. Liu *et al.*³² constructed a random forest regression model to screen stable perovskite oxides for solar cells. The model successfully filtered out 236 promising stable ferroelectric photovoltaic perovskite oxides with suitable band gaps from a pool of 4 058 905 candidate compositions with a coefficient of determination (R^2) of 0.932 and a root mean square error (RMSE) of 0.196 eV. Liu *et al.*²⁶ constructed classification models to screen stable and metastable perovskite oxides from ABO_3 compounds. They observed that a gradient boosting decision tree classifier outperformed its counterparts in accuracy, and the tolerance factor played the dominant role in differentiating perovskites from oxide compounds. 37 stable and 13 metastable perovskites were regarded as promising candidates for further investigation. Li *et al.*²² trained classification and regression models to project the thermodynamic stability and E_{h} values of perovskite oxides. The top-performing extra trees classification algorithm achieved an accuracy of around 0.93, whereas the leading kernel ridge regression model had a RMSE of approximately 28.5 meV atom⁻¹. Chen *et al.*³³ developed a particle swarm optimization-support machine regression (PSO-SVR) model to predict the E_{h} values of ABO_3 -type compounds. The R^2 and RMSE of the model were 0.957 and 87 meV atom⁻¹, respectively. YVO_3 , YNiO_3 , SrZrO_3 , RbPaO_3 , LaFeO_3 , and PrAlO_3 were predicted as stable perovskite oxides. Schmidt *et al.*³⁴ presented a ML strategy to predict the thermodynamic stability of solids including perovskites by predicting their E_{h} values. ML models trained on algorithms of ridge regression, random forests, extremely randomized trees, and neural networks, were applied to a dataset that contained around 250 000 cubic perovskites. They found that extremely randomized trees displayed the best performance, with a mean absolute error (MAE) of 121 meV atom⁻¹.

However, the black box nature of ML models poses a challenge in model interpretation. Herein, interpretable ML was applied to screen perovskite oxides from virtual perovskite-type combinations and extract scientific insights. The workflow of this study is shown in Fig. 2. Initially, five classification models were trained on an input dataset composed of 1133 single and double perovskite compounds^{14,28,35–37} that are described with 291 features. For feature selection, recursive feature elimination



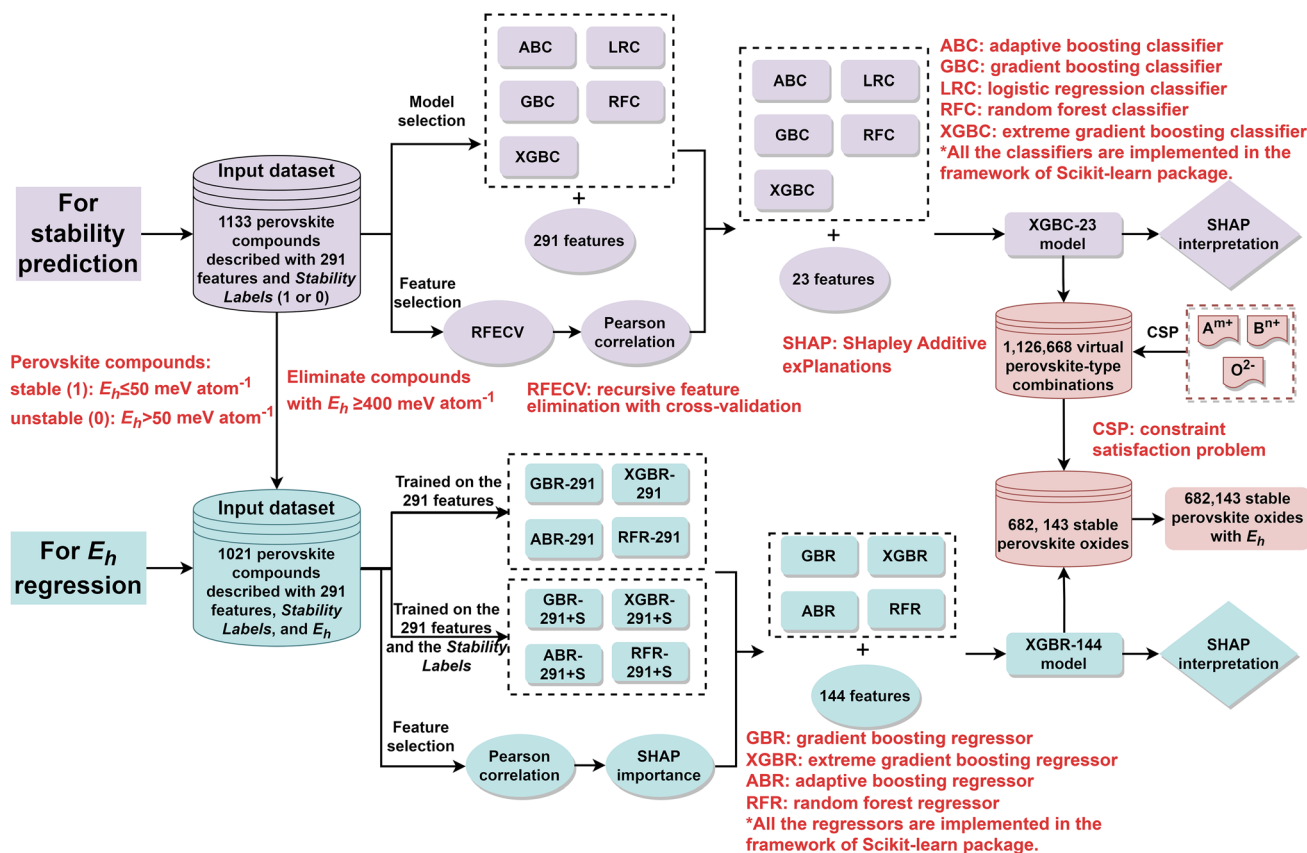


Fig. 2 The workflow of screening perovskite oxides by interpretable ML.

with cross-validation (RFECV) and Pearson correlation were successively applied to the 291 features, and 23 features were finally selected. After feature selection, five classification models were constructed on the optimal 23 features, and a XGBC-23 that outperformed its counterparts was then interpreted by SHapley Additive exPlanations (SHAP), which is a powerful tool for interpreting and understanding the predictions of ML models based on SHAP values which measures the contribution of each feature to the output of the models.³⁸ The model was thereafter utilized to screen stable perovskites from 1 126 668 virtual perovskite-type combinations that were generated by a constraint satisfaction problem (CSP) technique.¹² Afterward, various regression models, trained on an input dataset composed of 1021 perovskite compounds that were described with the 291 features, and the 291 features plus the stability label of the compounds, were constructed. It has to be noted that 112 compounds with E_h values of higher than 400 meV atom^{-1} were deleted for regression model training since we focus our attention on screen stable perovskite oxides. After Pearson correlation and SHAP importance investigation, 143 features were selected. Then, four regression models were constructed on 144 features (143 features and the stability label), and a XGBR-144 model which displayed the best performance. The model was then interpreted by SHAP, and the E_h values of 682 143 predicted stable perovskites were projected by it. It is believed that the models proposed in this study can be used to screen stable perovskite oxides for diverse applications,

such as perovskite-type electrode materials for solid oxide fuel cells and protonic ceramic fuel cells.

2. Experimental

An input dataset composed of 337 single perovskite compounds and 706 double perovskite compounds was collected for ML model training. The number of occurrences for each element in the perovskite compounds from the input dataset is shown in Fig. 3. 44 and 63 elements were, respectively, involved for the A- and B-sites. For the sake of uniformity, we recognized the appearance frequency for each A- and/or B-site element of single and symmetric double perovskites as two times. Hence, the overall number of appearances for the A-site or B-site was 2266 times. For the A-site, Ba was the most frequent element, followed by Sr, Ca, La, and Pb, which all of them appeared more than 100 times. Regarding the B-site, Mn was the most frequent element with 122 times, followed by Nb, Fe, Co, and Ta, which all of them appeared more than 90 times. The B-site elements were more scattered than the A-site elements, which is because more elements can occupy the B-site of perovskite oxides.³⁹

Each compound in the input dataset was described with 291 features, a stability label, and a E_h value. An E_h cutoff value of 50 meV atom^{-1} was used to separate stable and unstable perovskite compounds, where those with $0 \text{ meV atom}^{-1} \leq E_h \leq 50 \text{ meV atom}^{-1}$ and $E_h > 50 \text{ meV atom}^{-1}$ were labeled as stable (label 1) and unstable perovskite oxides (label 0), respectively.¹²



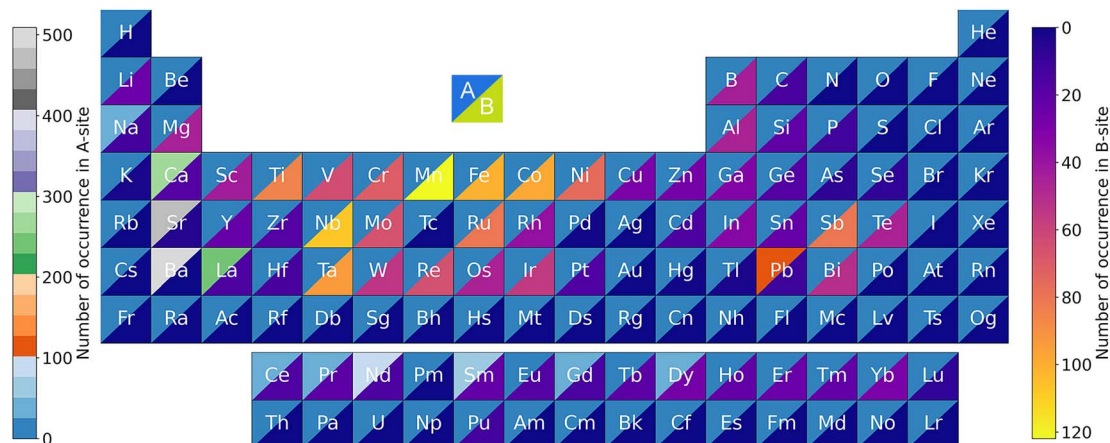


Fig. 3 Number of occurrences of the A- and B-site elements of the perovskite compounds in the input dataset.

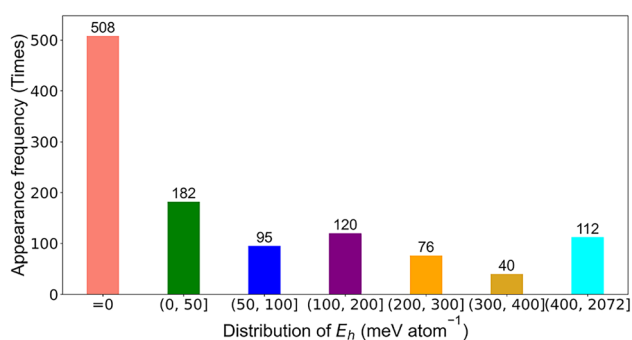


Fig. 4 The appearance frequency distribution of the E_h values of the perovskite compounds in the input dataset.

The appearance frequency distribution of the E_h values of the perovskite compounds in the input dataset is shown in Fig. 4. It can be seen that 508 samples had the E_h values of 0 meV atom^{-1} , while the E_h values of 182 samples were in the range of (0, 50) meV atom^{-1} , and 112 samples had the E_h values of bigger than 400 meV atom^{-1} . For regression model training, the compounds from the input dataset with E_h values of bigger than 400 meV atom^{-1} (112 compounds) were deleted since we

focused our attention on screening stable perovskite oxides. Therefore, 237 single perovskite compounds and 784 double perovskite compounds were adopted for regression model training.

The thermodynamic stability of perovskite oxides is fundamentally determined by their constituents, which manifest in their properties and interactions. Therefore, three types of fundamental features: geometric, atomic, and elemental features were employed for the A- and B-site elements (Table 1). Based on these three types of fundamental features, 291 features were generated. Since the A- and B-site cations of antisymmetric double perovskite oxides are different, supplementary features generated from the fundamental features except for TF, OF, IRR, and MF were introduced. For example, for the fundamental feature BP, 11 supplementary features were generated which were the boiling points of elements A and B ($A_1\text{-BP}$, $A_2\text{-BP}$, $B_1\text{-BP}$, $B_2\text{-BP}$), the average and mismatch boiling points of them (BP_{A^+} , BP_{A^-} , BP_{B^+} , BP_{B^-}), the average, difference, and ratio of the BP between them ($\text{BP}_{A-B_{\text{avg}}}$, $\text{BP}_{AB_{\text{diff}}}$, $\text{BP}_{AB_{\text{ratio}}}$). A_1 , A_2 , B_1 , and B_2 represent the A- and B-site elements of double perovskite oxides ($A_1A_2B_1B_2O_6$), respectively. For single perovskites (ABO_3), A_1 and B_1 are, respectively, the same as A_2 and B_2 . In addition, two

Table 1 Fundamental features that are introduced to generate the 291 features in this study

Types	Features
Geometric features	Tolerance factor (TF, t), ⁴⁰ octahedral factor (OF, μ), ⁴¹ the ratio of ionic radii ratio a to O (IRR, r_A/r_O), mismatch factor (MF), ³⁷ bond length (BL, \AA), atomic volume (AV, $\text{cm}^3 \text{mol}^{-1}$), ICSD (inorganic crystal structure database) volume (IV, \AA^3) ⁴²
Atomic features	Highest occupied molecular orbital energy (HOMO, eV), ³⁷ lowest unoccupied molecular orbital energy (LUMO, eV), ³⁷ ionic radius (IR, \AA), atomic weight (AW), covalent radius (CR, pm), ionization energy (IE, kJ mol^{-1}), atomic radius (AR, \AA), electron affinity (EA, kJ mol^{-1}), mendeleev number (MN), first ionization potential (FIP, V), electronegativity (EN), Zunger's pseudopotential radius (ZR, a.u.) ⁴³
Elemental features	Modulus of elasticity (ME, MMPa), boiling point (BP, K), melting point (MP, K), density (DT, kg m^{-3}), coefficient of thermal expansion (CTE, $\times 10^{-6} \text{K}^{-1}$), specific heat capacity (SHC, $\text{J g}^{-1} \text{K}^{-1}$), thermal conductivity (TC, $\text{W m}^{-1} \text{K}^{-1}$), electrical conductivity (EC, $\times 10^{-6} \text{m}^{-1} \Omega^{-1}$), the heat of fusion (HF, kJ mol^{-1}), the heat of vaporization (HV, kJ mol^{-1})
Complex features	$\Delta E_{\text{N}_{\text{AO}}} * \text{IRR}$, $\Delta E_{\text{N}_{\text{BO}}} * \text{OF}$



complex features: $\Delta E_{\text{N}_{\text{AO}}} * \text{IRR}$ and $\Delta E_{\text{N}_{\text{BO}}} * \text{OF}$ were also introduced.²⁶

Regarding feature selection for perovskite stability classification, a recursive feature elimination with cross-validation (RFECV) executed in the Scikit-learn package was employed to eliminate redundant features from the 291 features.⁴⁴ The pairwise Pearson correlate coefficients of the residual features were then calculated, and the features with strong correlations were abandoned. Finally, 23 features were used for classification model training (Table S1†). In terms of feature selection for E_{h} regression, the pairwise Pearson correlate coefficients of the 291 features were initially calculated, and the features with high correlations were deleted. Afterward, the importance of the remaining features was investigated by SHAP, and those with zero mean absolute SHAP values were eliminated. 143 features were finally singled out from the 291 features for regression model training.

To choose suitable algorithms for the prediction of the stability and E_{h} values of perovskite oxides, several different algorithms were employed to train classification and regression models. For classification models, an adaptive boosting classifier (ABC), gradient boosting classifier (GBC), logistic regression classifier (LRC), random forest classifier (RFC), and extreme gradient boosting classifier (XGBC) executed in the Scikit-learn package in Python were adopted.⁴⁴ Regarding the regression models, four algorithms: gradient boosting regressor (GBR), adaptive boosting regressor (ABR), random forest regressor (RFR), and extreme gradient boosting regressor (XGBR) in the framework of the Scikit-learn package in Python were utilized.⁴⁴ During model training, the input dataset was divided into training and testing datasets with a ratio of 75 : 25. Grid search with 10-fold cross-validation was employed to optimize the hyperparameters of the models. The hyperparameters for various classification and regression models are listed in Table S2.† During algorithm selection, statistical significance tests were executed in the SciPy package of Python for some models with similar performance. We employed *t*-test to assess the significance of differences in accuracy and R^2 among the tested classification and regression algorithms, respectively. The significance level was set at 0.05.

For classification models, five indices: accuracy, precision, recall, F1-score and area under the receiver operating characteristic (ROC) curve (AUC) calculated from binary confusion matrices were used to evaluate their performance. The binary confusion matrix is a two-dimensional table, of which the rows and columns represent the actual and predicted classes that the perovskite compounds belong to, respectively. Therefore, four types of results: true positives (TP), false negatives (FN), false positives (FP), and true negatives (TN) are included in the matrix.¹² The formulas of the four indices are shown in eqn (5)–(8). Accuracy refers to the proportion of correct predictions made by the classification models, while precision and recall measure the percentage of TP out of all predicted positives and actual positives, respectively. Regarding F1-score, it is calculated as the harmonic mean of precision and recall, which attempts to strike a balance between them. A ROC curve, plotting the true positive rate (TPR, eqn (9)) against the false

positive rate (FPR, eqn (10)) at different thresholds, depicts the performance of a classification model at all discrimination thresholds.

In terms of the regression models, three indices: R^2 , RMSE and MAE were employed to evaluate their quality.^{45,46} R^2 is a measure of how accurately regression models can predict unseen instance. A higher R^2 value indicates better model performance and overall quality. RMSE is a commonly used index for indicating the accuracy of regression models, as it quantifies the discrepancies between predicted values and actual values. MAE is the average of the absolute differences between practical and forecasted values. The formulas for these three indices are shown in eqn (11)–(13), where y_i and \tilde{y}_i are the actual values and predicted values of the i th instance in the testing dataset, respectively, \bar{y} is the mean actual values of all the n instances.

$$\text{Accuracy} = \frac{\text{TP} + \text{TN}}{\text{TP} + \text{FN} + \text{FP} + \text{TN}} \quad (5)$$

$$\text{Precision} = \frac{\text{TP}}{\text{TP} + \text{FP}} \quad (6)$$

$$\text{Recall} = \frac{\text{TP}}{\text{TP} + \text{FN}} \quad (7)$$

$$\text{F1-score} = \frac{2 \times \text{precision} \times \text{recall}}{\text{precision} + \text{recall}} \quad (8)$$

$$\text{TPR} = \frac{\text{TP}}{\text{TP} + \text{FN}} \quad (9)$$

$$\text{FPR} = \frac{\text{FP}}{\text{FP} + \text{TN}} \quad (10)$$

$$R^2 = 1 - \frac{\sum_1^n (y_i - \tilde{y}_i)^2}{\sum_1^n (y_i - \bar{y}_i)^2} \quad (11)$$

$$\text{RMSE} = \sqrt{\frac{\sum_1^n (y_i - \tilde{y}_i)^2}{n}} \quad (12)$$

$$\text{MAE} = \frac{\sum_1^n |y_i - \tilde{y}_i|}{n} \quad (13)$$

To screen potential single and double perovskite oxides from previously unseen instances, virtual perovskite-type combinations with symmetric and antisymmetric double perovskite compounds were generated using a constraint satisfaction problem (CSP) technique under the restrictions of charge neutrality and Goldschmidt tolerance factor t , which had been reported in our previous study.¹² It should be emphasized that the symmetric virtual double perovskite-type combinations were regarded as single perovskite-type combinations. Since the t values of perovskite oxides are normally in the range of 0.89 to



1.06,⁴⁷ we limited it to the range of 0.90 to 1.10 during virtual combinations generation.

3. Results and discussion

3.1 Perovskite stability classification

The performance of the classification models trained on the 291 features is shown in Fig. 5(a) and Table 2. The XGBC model outperforms its counterparts. The accuracy, precision, recall, F1-score, and the receiver operating characteristic (ROC) curves (AUCs) of it were 0.908, 0.922, 0.932, 0.927, and 0.970, respectively. Achieving identical results in accuracy (0.901), precision (0.916), recall (0.921), and F1-score (0.927), the GBC and LRC models diverged only in their AUCs, with values of 0.968 and 0.937, respectively. Regarding the ABC and RFC models, they yielded similar results in terms of accuracy, recall, and AUC. However, a distinction emerged in their precision and F1-score, with the ABC model achieving 0.935 and 0.898, respectively, and

Table 2 Performance of the classification models trained on the 291 features

Algorithms	Accuracy	Precision	Recall	F1-score	AUC
ABC	0.898	0.935	0.916	0.898	0.958
GBC	0.901	0.916	0.921	0.927	0.968
LRC	0.901	0.916	0.921	0.927	0.937
RFC	0.898	0.925	0.917	0.910	0.964
XGBC	0.908	0.922	0.932	0.927	0.970

the RFC model attaining 0.925 and 0.910, respectively. During the training of these models, default hyperparameters of these algorithms were used. Given the comparable performance of the GBC and XGBC models, a statistical significance test (*t*-test) was conducted to assess their difference. The *p*-value for it was 0.00195, indicating that there was a significant difference between the two algorithms.

Concerning feature selection for classification, 34 features were singled out from the 291 features (Table S1†). The pairwise Pearson correlation coefficient heatmap of them was investigated (Fig. S1†). It was found that 17 pairs of them were with strong correlations. For instance, the pairwise coefficient between AR_AB_avg and IV_AB_avg is 0.99. Thus, 11 of the 34 features (Table S1†) were removed, and the pairwise Pearson correlation coefficient heatmap of the 23 optimal features is shown in Fig. 5b. Apart from geometrical and atomic properties, elemental properties such as modulus of elasticity of elements A and B were also essential in predicting the thermodynamic stability of perovskite oxides. Moreover, out of the 23 features, 14 of them involved the characteristics of both the A- and B-site elements, 9 features engaged the attributes of the B-site elements, while none of the features exclusively pertained to the A-site elements. This indicated that the perovskite stability was determined by the attributes of the A- and B-site elements, especially for the B-site elements.

After model and feature selection, an XGBC-based classification model named XGBC-23 was trained on the 23 features for perovskite stability prediction. The resulting confusion matrix and ROC curve are shown in Fig. 6. In comparison with the XGBC model trained with the 291 features, the XGBC-23 model provided improved accuracy, precision, recall, and F1-score, which were 0.919, 0.937, 0.935, and 0.932, respectively. Regarding the AUC, it was 0.969 for the XGBC-23 model, which was comparable to the XGBC model trained with 291 features, indicating its excellent performance in distinguishing thermodynamically stable and unstable perovskite oxides.

Classification models trained on the 23 features using ABC, LRC, GBC, and RFC algorithms were also constructed. The hyperparameters of these models were tuned using grid search with 10-fold cross-validation (Table S2†). According to Table 3, the XGBC-23 model still displayed the best performance. All the evaluation metrics of the ABC-23, GBC-23, and RFC-23 models witnessed a little bit of decrease compared to their counterparts that trained on the 291 features. However, the performance of the LRC-23 model observed a dramatic decrease as compared to the LRC model trained on the 291 features. The accuracy,

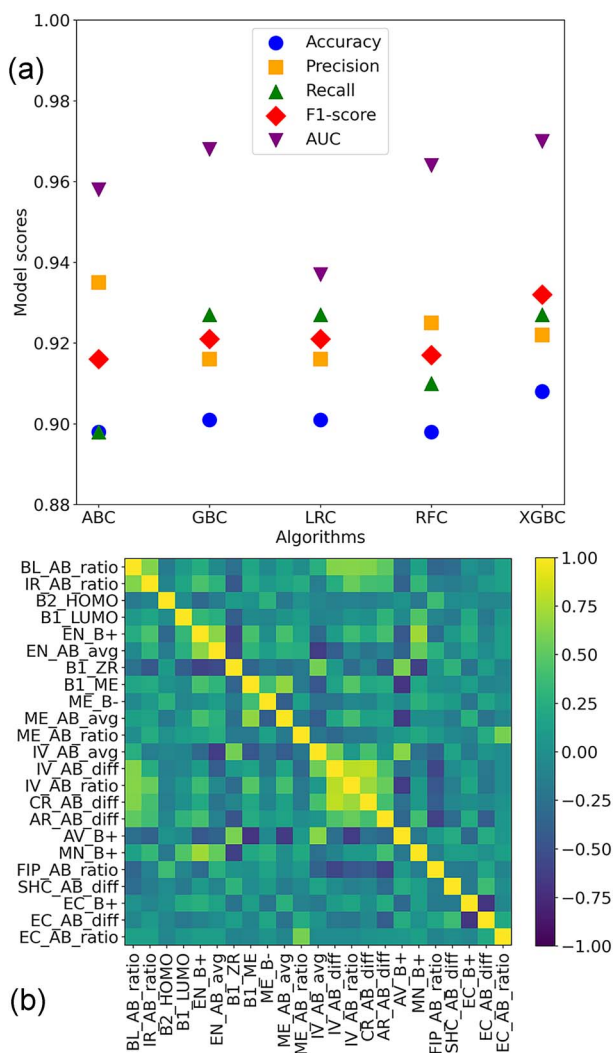


Fig. 5 (a) Performance of the classification models trained on the 291 features. (b) Pairwise Pearson correlation coefficient heatmap of the 23 features.



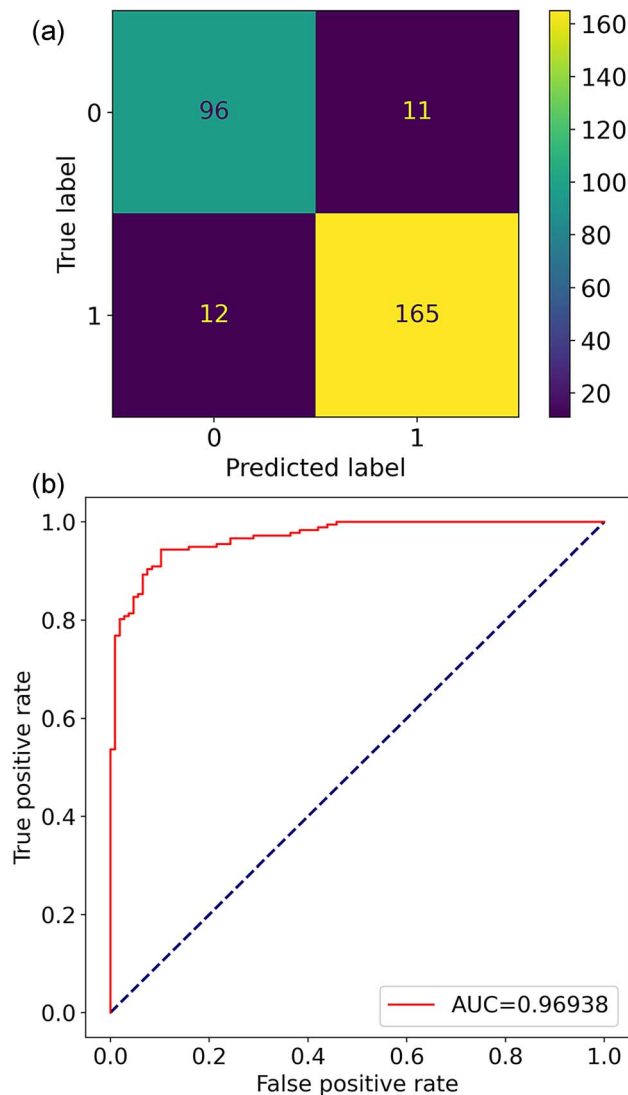


Fig. 6 (a) The confusion matrix and (b) ROC curve of the XGBC-23 model.

precision, recall, F1-score, and AUC declined from 0.901, 0.916, 0.921, 0.927, and 0.937 to 0.732, 0.767, 0.819, 0.792, and 0.831, respectively. The confusion matrices and ROC curves of the ABC-23, GBC-23, LRC-23, and RFC-23 models can be seen in Fig. S2,† S3. Since the GBC-23 and XGBC-23 models had similar performance, a statistical significance test (t -test) was executed for them. The p -value for it was 0.00391, implying the significant

Table 3 Performance of various classification models for perovskite stability prediction

Algorithms	Accuracy	Precision	Recall	F1-score	AUC
ABC-23	0.873	0.908	0.887	0.897	0.927
GBC-23	0.908	0.931	0.921	0.926	0.969
LRC-23	0.732	0.767	0.819	0.792	0.831
RFC-23	0.898	0.916	0.921	0.918	0.961
XGBC-23	0.919	0.937	0.935	0.932	0.969
XGBC-ref. 22	0.917	0.924	0.803	0.859	0.959

difference between the two algorithms. Therefore, the XGBC-23 model can be a promising candidate for screening stable perovskite oxides from perovskite-type compounds.

The XGBC-23 model of this study even displayed better performance than the XGBC-ref model (Table 3 and Fig. S4†). More specifically, the two models obtained similar results in accuracy and AUC. Nevertheless, the precision (0.924), recall (0.803), and F1-score (0.859) of the XGBC-ref model were lower than that of the XGBC-23 model. Therefore, the XGBC-23 model can be a promising candidate for screening stable perovskite oxides from perovskite-type compounds.

To explore the importance and interactions of the 23 features, SHAP was employed to interpret the XGBC-23 model (Fig. 7). Fig. 7(a) displays the SHAP feature importance of the 23 features. In contrast to their counterparts, B2_HOMO, B1_ME, and IV_AB_diff exhibited pronounced significance, as evidenced by their mean absolute SHAP values (MASVs) exceeding 0.8, indicating the predominant role of the electron loss capability and the elastic modulus of the B-site elements, and the ICSD volume difference between atoms A and B in determining the thermodynamic stability of perovskite oxides. After them, the next eight features, which consider properties related to the A- and B-site elements, including IV_AB_ratio, CR_AB_diff, and IV_AB_avg, exhibited notable importance, each demonstrating MASVs surpassing 0.4. Nevertheless, FIP_AB_ratio, AV_B+, and EC_B+ were discerned to exhibit minimal significance, each characterized by MASVs of less than 0.2.

Shown in Fig. 7(b) is the SHAP summary plot for the XGBC-23 model. Each dot in the figure represents a perovskite compound per feature. Its position on the x-axis is determined by its SHAP value. The y-axis indicates the features, in order of importance from top to bottom. Overlapping dots shift in the y-axis direction. The color of a dot from red to blue denotes its feature value from high to low. A positive SHAP value for a feature means that the feature has a positive impact on the model prediction, whereas a negative SHAP value for a feature indicates the feature deteriorates the model prediction.

According to Fig. 7(b), medium B2_HOMO promoted the thermodynamic stability of perovskite oxides. Since HOMO is the orbital with the highest energy that contains electrons, and its energy equals the minus vertical ionization potential that describes the minimum energy required to remove an electron from an atom, without changing its geometry,^{48–51} the stability of perovskite oxides is negatively impacted by either excessively reactive or highly inert B-site atoms.

Perovskite oxides are not strictly ionic, they possess a notable covalent nature in their bonds.³⁶ ME quantifies bond stiffness, a property strongly influenced by bond length.⁵² Shorter and stronger bonds contribute to a stiffer lattice, resulting in higher ME values.⁵² Since the B-site cations are in 6-fold coordination with the oxygen ions in the perovskite structure forming BO₆ octahedra, a higher B-site modulus (B1_ME) means the BO₆ octahedra are less deformable and better able to maintain the geometry required for stability. Due to the typically A-site rare-earth, alkaline, or alkaline-earth metals have lower ME than the normally B-site transition metals, lower ME_AB_ratio pushes the stability of perovskite



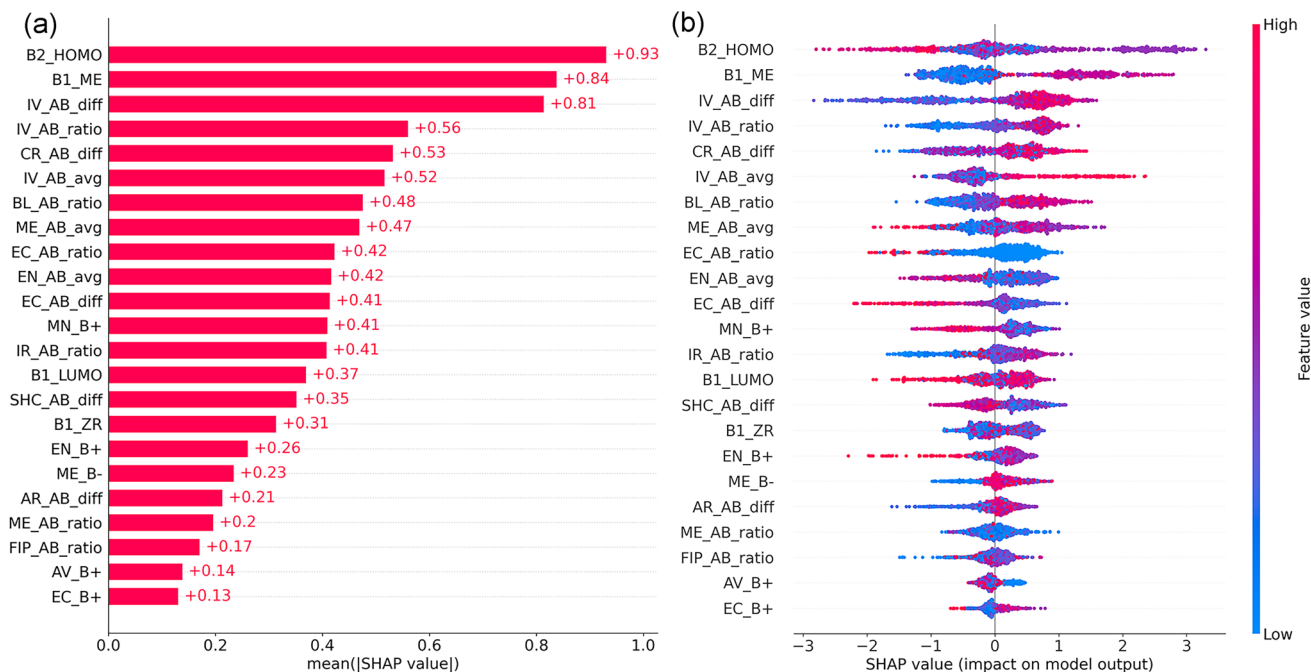


Fig. 7 (a) SHAP feature importance, and (b) summary plot for the XGBC-23 model.

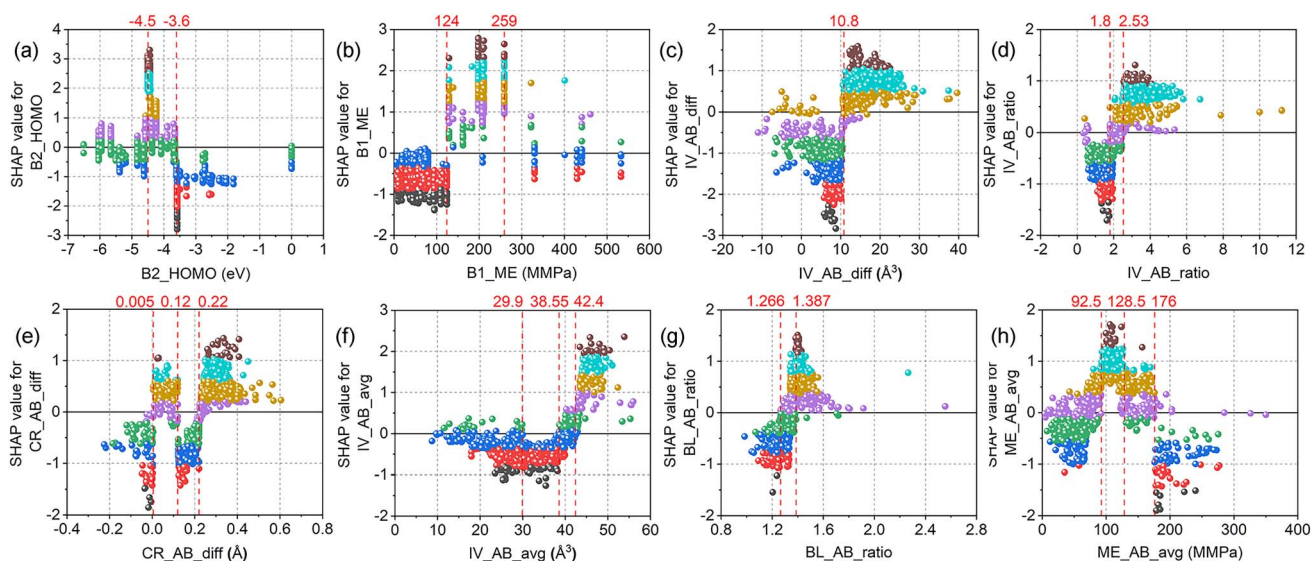


Fig. 8 SHAP dependence plots of the top eight features for perovskite stability prediction: (a) B2_HOMO, (b) B1_ME, (c) IV_AB_diff, (d) IV_AB_ratio, (e) CR_AB_diff, (f) IV_AB_avg, (g) BL_AB_ratio, (h) ME_AB_avg.

oxides. Additionally, a balance can be struck between the lower ME of the A-site element and the bigger ME of the B-site element, where a moderate ME_AB_avg promoted the stability of perovskite oxides.

For the perovskite structure, the atom A and A-O bond length are usually larger and longer than the atom B and B-O bond length;^{15,53} therefore, greater feature values of IV_AB_diff, IV_AB_ratio, IV_AB_avg, CR_AB_diff, BL_AB_ratio, IR_AB_ratio, and AR_AB_diff, and lower feature values of AV_B+ were beneficial to the stability of perovskite oxides.

The electronegativities of the elements occupying the A- and B-sites in perovskite oxides are typically lower than that of oxygen. Therefore, the covalent or ionic nature of the A-O and B-O bonds is dictated by the difference in electronegativity between the A/B elements and oxygen.⁵⁴ It has been observed that the ionic character of the A-O bond contributes to the stabilization of the cubic perovskite structure.⁵⁵ Thus, elements at the A-site with lower electronegativity and larger cation size are conducive to the stability of the cubic perovskite structure.⁵⁵ Given that the B-site element is generally more electronegative than the A-site



element, the B–O interaction is typically stronger than the A–O interaction.⁵⁵ B-site elements with relatively lower electronegativity may not form a B–O bond that is strong enough to maintain a stable perovskite structure. Conversely, B-site elements with higher electronegativity could induce distortions due to octahedral tilting.⁵⁵ Hence, medium EN_{B+} and EN_{AB_avg} are advantageous for the stability of cubic perovskite oxides.

SHAP dependence plots of the top eight features for the XGBC-23 model are illustrated in Fig. 8. As can be seen in Fig. 8(a), perovskite oxides with B-site elements having B2_HOMO above -3.6 eV (e.g., Ru, Rh) tended to be unstable, while those with B2_HOMO at around -4.5 eV (e.g., Mn, Ni) were prone to be stable, as evidenced by the highest SHAP values obtained at B2_HOMO = -4.5 eV. In terms of B1_ME (Fig. 8(b)), most of the SHAP values were negative and positive when it was lower than 124 MMPa (e.g., Cu, Zr) and in the range of 124 to 259 MMPa (e.g., V, Mn), respectively. However, positive and negative SHAP values coexisted when B1_ME is higher than 330 MMPa (e.g., Rh, Ru). Regarding IV_AB_diff (Fig. 8(c)), two distinct regions with positive and negative SHAP values were observed. The ICSD volume differences between atoms A and B that were greater than 10.8 \AA^3 (e.g., Ba₂GdBiO₆, Sr₂CaOsO₆) were favorable for the stability of perovskite oxides. On the contrary, the perovskite stability deteriorates when IV_AB_diff was lower than 10.8 \AA^3 (e.g., PrSrLiTeO₆, Nd₂MgPtO₆). However, some exceptions with IV_AB_diff of lower than 10.8 \AA^3 had positive SHAP values, taking MnGeO₃ (IV_AB_diff = -5 \AA^3) as an example. For IV_AB_ratio (Fig. 8(d)), the SHAP values were positive and negative when it was higher than 2.53 (e.g., SrTiO₃, Sr₂GaNbO₆) and lower than 1.80 (e.g., TmTiO₃, La₂CaZrO₆), respectively. A transition zone was also witnessed with positive and negative SHAP values coexisting. Therefore, the perovskite stability can be stimulated by a higher IV_AB_ratio. Concerning CR_AB_diff (Fig. 8(e)), the perovskite stability was promoted when it was in the range of 0.005 to 0.12 \AA (e.g., PbZrO₃, Pb₂-CoMoO₆), and higher than 0.22 \AA (e.g., EuAlO₃, Ba₂LaPuO₆). However, when it was in the range of 0.12 to 0.22 \AA , and lower than 0.005 \AA , the SHAP values were negative, and therefore the stability of perovskites was ruined. Regarding IV_AB_avg (Fig. 8(f)), all the SHAP values were positive when IV_AB_avg was higher than 42.4 \AA^3 (e.g., Ba₂SrTeO₆, Sr₂YbSbO₆), while all the SHAP values were negative when IV_AB_avg was in the range of 29.9 to 38.55 \AA^3 (e.g., LaSrCuSbO₆, BaLaMgNbO₆). Two overlapping zones with positive and negative SHAP values coexisting were also presented. For BL_AB_ratio (Fig. 8(g)), higher SHAP values were obtained when it was at around 1.4 (e.g., Ba₂-HoRuO₆, Ba₂CeSnO₆), while the SHAP values were negative when it was lower than 1.266. A transition zone was also observed where the SHAP values underwent a transition from negative to positive. About ME_AB_avg (Fig. 8(h)), positive SHAP values were acquired when the feature values were greater than 92.5 MMPa and lower than 128.5 MMPa. Negative SHAP values were obtained when ME_AB_avg was higher than 176 MMPa. However, when the feature values were outside the range of 92.5 to 128.5 MMPa, negative and positive SHAP values were both observed.

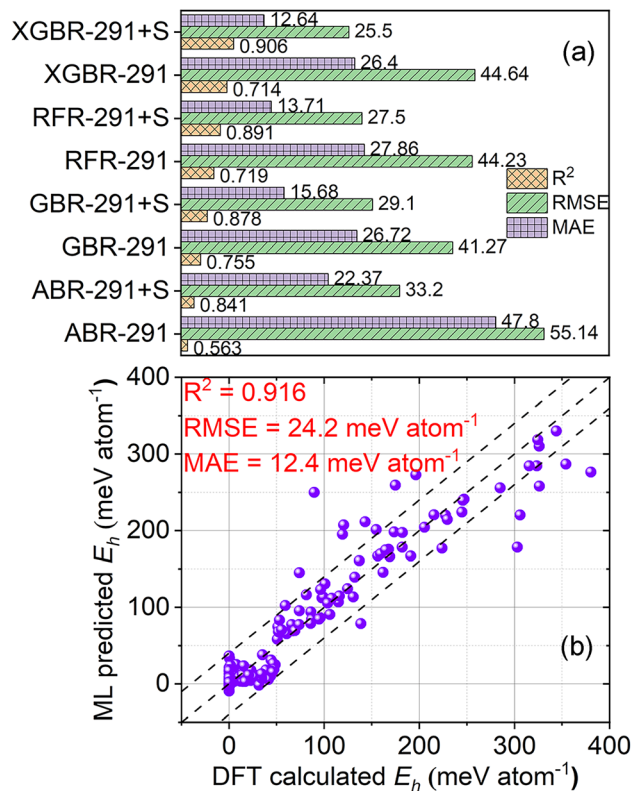


Fig. 9 (a) Performance of the regression models trained on the 291 features (ABR-291, GBR-291, RFR-291, XGBR-291) and the 291 features and the stability label (ABR-291 + S, GBR-291 + S, RFR-291 + S, XGBR-291 + S), respectively. (b) Performance of the XGBR-144 model.

3.2 Perovskite E_h value regression

For regression algorithm selection, regression models that were trained on the 291 features and the 291 features and the stability label were constructed. As depicted in Fig. 9(a), the GBR-291 model demonstrated the highest R² of 0.755 and the lowest RMSE of $41.27 \text{ meV atom}^{-1}$. Despite having lower R² and higher RMSE values compared to the GBR-291 model, the XGBR-291 model had a slightly lower MAE (MAE = $26.40 \text{ meV atom}^{-1}$) than the GBR-291 model (MAE = $26.72 \text{ meV atom}^{-1}$). The RFR-291 and XGBR-291 models yielded similar R² and RMSE, while the performance of the ABR-291 model was inferior to other regression models. With the addition of the stability label as a feature for model training, the performance of the regression models was significantly enhanced. For

Table 4 Performance of various regression models for E_h regression

Algorithms	R ²	RMSE (meV atom ⁻¹)	MAE (meV atom ⁻¹)
RFR-144	0.893	27.3	13.9
GBR-144	0.896	26.8	14.3
ABR-144	0.876	29.3	17.5
XGBR-144	0.916	24.2	12.4
XGBR-ref. 22	0.781	46.63	21.96



example, compared to the GBR-291 model, the GBR-291 + S model had an increased R^2 of 0.878, and decreased RMSE and MAE of 29.1 and 15.68 meV atom⁻¹, respectively. The most notable improvement was seen in the XGBR-291 + S model, which exhibited the best performance after the introduction of the stability label for model training. Its R^2 , RMSE, and MAE were 0.906, 25.5 meV atom⁻¹, and 12.64 meV atom⁻¹, respectively.

For feature selection, 143 features were finally singled out from the 291 features. Therefore, an XGBR-144 regression model for predicting the E_h values of perovskite oxides was developed on the 143 features and the stability label (Fig. 9(b) and Table 4). The R^2 , RMSE, and MAE of the model were 0.916, 24.2 meV atom⁻¹, and 12.4 meV atom⁻¹, respectively. The performance of the XGBR-144 model is comparable to or better than previously reported models for E_h regression.^{22,33,34,56} One of the reasons may be attributed to the adoption of the stability label as one of the features for regression model training.

To provide a more rigorous comparison, we also constructed regression models of RFR-144, GBR-144, and ABR-144 using the RFR, GBR, and ABR algorithms on the 143 features and the stability label, respectively, and a regression model of XGBR-ref using the XGBR algorithm on the features of ref. 22, as displayed in Fig. S5, S6† and Table 4. The XGBR-144 model exhibited the best performance among all the regression models. The RFR-144 and GBR-144 models displayed comparable performance in all three metrics, while the ABR-144 showed the worst performance in the four models of this study. In light of the analogous performance demonstrated by the GBR-144 and XGBR-144 models, a statistical significance test, specifically a *t*-test, was employed to appraise potential distinctions between them. The *p*-value for it was 2.67×10^{-10} ,

which indicated the significant differences between the two algorithms. In terms of the XGBR-ref model, its R^2 , RMSE, and MAE were 0.781, 46.63 meV atom⁻¹, and 21.96 meV atom⁻¹, respectively.

Fig. 10a presents the SHAP feature importance of the top ten features for the XGBR-144 model. The stability label was the most important feature, with a MASV of 0.0653. Given the overall MASV for all features was 0.1291, the stability label accounted for 50.58%. Besides the stability label, IR_AB_diff, BL_AB_diff, and A2_ME were three of the most important features. Therefore, the ionic radius difference between the A- and B-site cations, the A-O and B-O bond length difference, as well as the elastic modulus of the A-site elements, were all significant indicators for E_h values of perovskite oxides. Furthermore, among the top ten features, the fundamental features of ME and IR were involved four and two times, respectively, revealing their significant roles in predicting the E_h values of perovskite oxides.

Fig. 10b illustrates the SHAP summary plot of the ten features for the XGBR-144 model. The SHAP values of the stability label that is 1 or 0 were all negative or positive, respectively, because stable perovskites had lower E_h values than unstable ones. Higher IR_AB_diff and BL_AB_diff pushed the decrease of E_h values. This phenomenon can be explained by the fact that the A-site cations typically have a larger ionic radius and a longer A-O bond length compared to the B-site cations and their corresponding B-O bond length. Moreover, the lower elastic modulus of the A-site elements (A2_ME and A1_ME) also promoted the reduction of the E_h values of perovskite oxides. This can be explained by the necessity for A-site elements to be flexible in accommodating variations in the sizes and positions of the surrounding BO₆ octahedra. Reduced

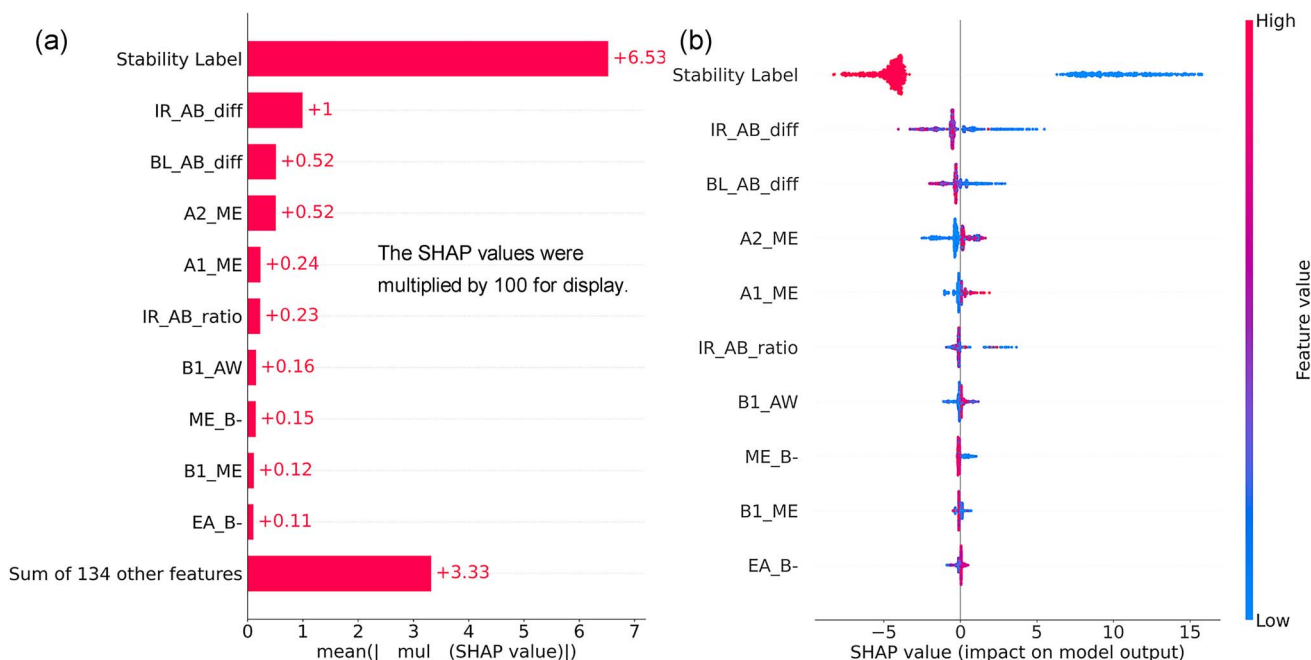


Fig. 10 SHAP feature importance (a) and summary plot (b) of the top ten features of the XGBR-144 model.



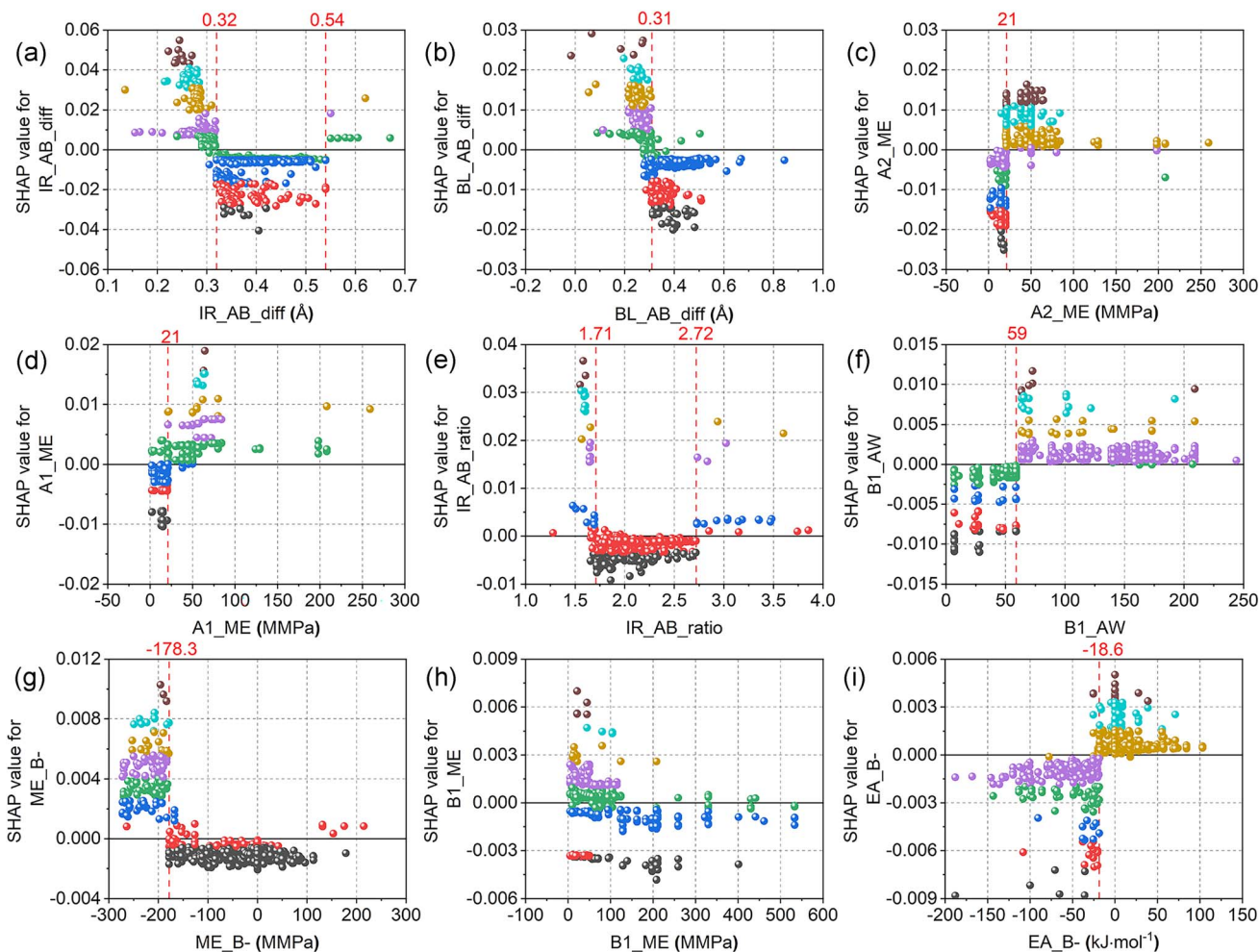


Fig. 11 SHAP dependence plots of the top nine features of the XGBR-144 model: (a) IR_AB_diff, (b) BL_AB_diff, (c) A2_ME, (d) A1_ME, (e) IR_AB_ratio, (f) B1_AW, (g) ME_B-, (h) B1_ME, (i) EA_B-.

values of B1_AW and EA_B-, as well as medium IR_AB_ratio and increased ME_B-, had a beneficial effect in lowering the E_h values of perovskite oxides.

In Fig. 11, the SHAP dependence plots of the nine most important features of the XGBR-144 model are displayed. More specifically, when the ionic radius difference between elements A and B (IR_AB_diff, Fig. 11(a)) was greater than 0.32 Å (e.g., BaTeO₃, La₂MgZrO₆) and lower than 0.54 Å (e.g., BaMnO₃, Ba₂CoIrO₆), the SHAP values were negative and therefore stimulated the reduction of E_h values. Similarly, almost all the SHAP values were negative when IR_AB_ratio (Fig. 11(e)) was greater than 1.71 (e.g., YbTiO₃, La₂NaIrO₆) and lower than 2.72 (e.g., SrCoO₃, Sr₂CoMnO₆). From this, it can be inferred that the reduction of E_h values was aided by moderate IR_AB_diff and IR_AB_ratio. For BL_AB_diff (Fig. 11(b)), when the feature values were greater than 0.31 Å (e.g., Pb₂FeTaO₆, CeVO₃), most of the SHAP values were negative; therefore, perovskites with longer A–O and shorter B–O bond lengths had lower E_h values. In terms of A2_ME (Fig. 11(c)) and A1_ME (Fig. 11(d)), when the feature values were less than 21 MMPa (e.g., Pb, Yb, Sr), the majority of the SHAP values were negative, which assist in the

reduction of the E_h values. Looking at Fig. 11(f), the graph was split into two sections with positive and negative SHAP values by a boundary line at B1_AW = 59. Thus, adopting elements with atomic weights of less than 59 (e.g., Co, Ni, Fe) at the B-site bolstered the decrease of the E_h values. As shown in Fig. 11(g), a demarcation line at ME_B- = -178.3 MMPa divided the graph into two parts. When the feature values were greater than -178.3 MMPa (e.g., NaGdMgWO₆, Ca₂CoOsO₆), practically all the SHAP values were negative. There is, however, no clear dividing line to separate Fig. 11(h) (B1_ME) into different regions with positive and negative SHAP values, which suggests that ME_B- can offer more information than B1_ME in predicting the E_h values of perovskites. For EA_B- (Fig. 11(i)), almost all the SHAP values were negative when it was lower than -18 kJ mol⁻¹ (e.g., LaSrCoRuO₆, Ba₂TmBiO₆). This facilitates the reduction of the E_h values of perovskites.

3.3 Classification and regression model generalization

We applied the XGBC-23 and XGBR-144 models to the 1 126 668 virtual perovskite-type combinations, expecting to predict their stability and E_h values, respectively. It was found that 682 143 of



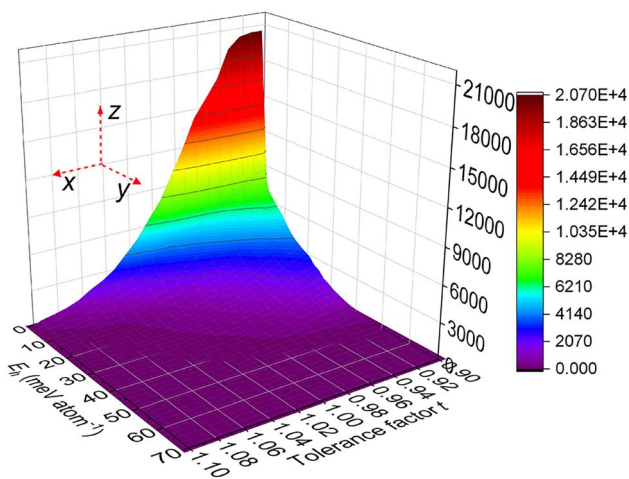


Fig. 12 The relationship between the E_h values of the projected stable perovskite oxides and their tolerance factor t in terms of numerical count.

the combinations were identified as stable perovskite oxides by the XGBC-23 model, and practically all the predicted stable perovskites were projected with E_h values less than 50 meV atom^{-1} by the XGBC-144 model, including 141 545 of them having zero E_h values. Fig. 12 displays the E_h values of the projected stable perovskites related to their tolerance factor t in terms of numerical count (z -axis). The number of stable perovskites decreased with the increase of t and E_h values. Most of the stable perovskites were in the corner of the graph, where their t and E_h values of them were, respectively, in the range of 0.90 to 1.02 and 0 to 32 meV atom^{-1} .

Shown in Fig. 13 is the appearance frequency of the A- and B-site elements in the periodic table of the 682 143 predicted stable perovskite oxides with E_h values of lower than 50 meV atom^{-1} . The percentage of the element accommodated on the A- and B-site is revealed by the color of the triangle. It can be seen that K, Rb, Cs, Ba, Nd, Sm, Eu, and Tl had higher possibilities than their counterparts to accommodate at the A-site.

Regarding the B-site elements, transition metal Cr exhibited the highest frequency. Other transition metals, *e.g.* V, Mn, Fe, Co, Ni, also had high possibilities to be the B-site elements of stable perovskite oxides. Despite being pivotal elements for the A-site, alkali metals K, Rb, and Cs cannot function as the B-site elements, presumably due to their large ionic radius.

To verify the efficacy of the XGBC-144 model, the E_h values of some predicted stable perovskite oxides that have been experimentally investigated and/or DFT calculated were compared with those in the Materials Project (MP) database, as displayed in Table S3.† For example, Fe-, Co-, and Mn-based double perovskite oxides have been enormously used as the electrode materials of solid oxide fuel cells and protonic ceramic fuel cells,^{57–59} and electrocatalysts for oxygen evolution.⁶⁰ Bismuth-based double perovskite oxides were employed as photocatalysis.^{61,62} It can be found that the predicted stable perovskite oxides in this study had E_h values like those in the MP database. For instance, the E_h values of a double perovskite photocatalyst $\text{Ba}_2\text{BiLaO}_6$ (ref. 61) that was projected by the regression model and calculated by DFT were 28 and 30 meV atom^{-1} , respectively. Double perovskite BaSrCoWO_6 had been investigated as a parent structure for solid oxide fuel cell cathode materials,⁶³ its E_h values predicted by the XGBC-144 model and calculated by DFT were 15 and 0 meV atom^{-1} , respectively. Moreover, in our input dataset, there was no double perovskite oxide having the composition of $\text{Eu}_2\text{B}'\text{B}''\text{O}_6$. However, the E_h values predicted by the XGBC-144 model exhibited strong alignment with those calculated by DFT. Therefore, the XGBC-144 model developed in this work demonstrated excellent performance in predicting the E_h values of perovskite oxides.

4. Conclusions

In summary, interpretable machine learning is applied to screen perovskite oxides from virtual perovskite-type combinations. The extreme gradient boosting algorithm outperformed its counterparts in predicting the thermodynamic stability and E_h values of perovskite oxides. The XGBC-23 classification model achieved an accuracy of 0.919, precision of 0.937, F1-

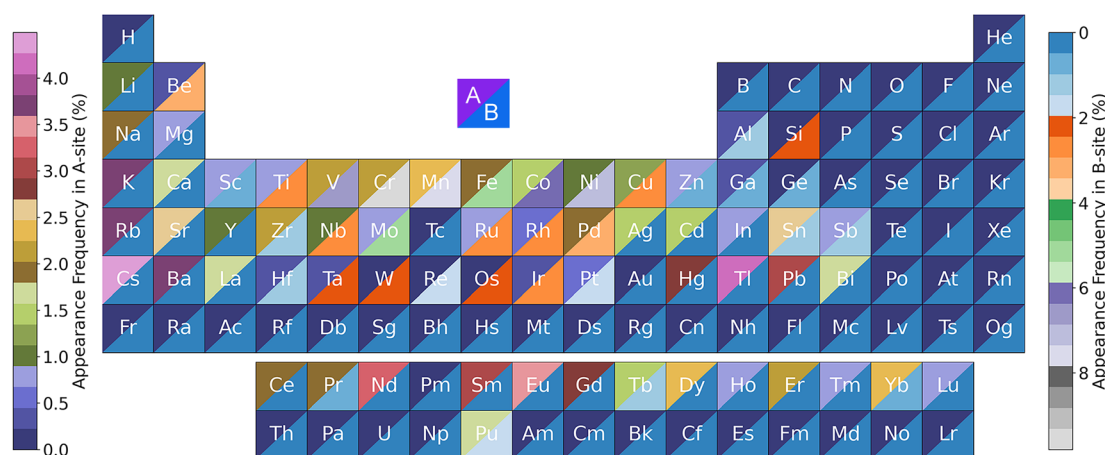


Fig. 13 The appearance frequency of the A- and B-site elements of the 682 143 predicted stable perovskite oxides with E_h values of lower than 50 meV atom^{-1} .



- 34 J. Schmidt, J. Shi, P. Borlido, L. Chen, S. Botti and M. A. L. Marques, *Chem. Mater.*, 2017, **29**, 5090–5103.
- 35 A. Jain, S. P. Ong, G. Hautier, W. Chen, W. D. Richards, S. Dacek, S. Cholia, D. Gunter, D. Skinner and G. Ceder, *APL Mater.*, 2013, **1**, 011002.
- 36 S. Vasala and M. Karppinen, *Prog. Solid State Chem.*, 2015, **43**, 1–36.
- 37 A. Talapatra, B. P. Uberuaga, C. R. Stanek and G. Pilania, *Chem. Mater.*, 2021, **33**, 845–858.
- 38 S. M. Lundberg and S.-I. Lee, *Adv. Neural Inf. Process. Syst.*, 2017, **30**, 4765–4774.
- 39 L. G. Tejuca, J. L. G. Fierro and J. M. D. Tascón, in *Advances in Catalysis*, ed. D. D. Eley, H. Pines and P. B. Weisz, Academic Press, 1989, vol. 36, pp. 237–328.
- 40 V. M. Goldschmidt, *Naturwissenschaften*, 1926, **14**, 477–485.
- 41 C. Li, X. Lu, W. Ding, L. Feng, Y. Gao and Z. Guo, *Acta Crystallogr., Sect. B*, 2008, **64**, 702–707.
- 42 L. Ward, A. Agrawal, A. Choudhary and C. Wolverton, *NPJ Comput. Mater.*, 2016, **2**, 16028.
- 43 A. Zunger, *Phys. Rev. B: Condens. Matter Mater. Phys.*, 1980, **22**, 5839.
- 44 F. Pedregosa, G. Varoquaux, A. Gramfort, V. Michel, B. Thirion, O. Grisel, M. Blondel, P. Prettenhofer, R. Weiss, V. Dubourg, J. Vanderplas, A. Passos, D. Cournapeau, M. Brucher, M. Perrot and É. Duchesnay, *J. Mach. Learn. Res.*, 2011, **12**, 2825–2830.
- 45 V. Gladkikh, D. Y. Kim, A. Hajibabaei, A. Jana, C. W. Myung and K. S. Kim, *J. Phys. Chem. C*, 2020, **124**, 8905–8918.
- 46 X. Yang, L. Li, Q. Tao, W. Lu and M. Li, *Comput. Mater. Sci.*, 2021, **196**, 110528.
- 47 S. Afroze, A. Karim, Q. Cheok, S. Eriksson and A. K. Azad, *Front. Energy*, 2019, **13**, 770–797.
- 48 T. Tsuneda, J.-W. Song, S. Suzuki and K. Hirao, *J. Chem. Phys.*, 2010, 133.
- 49 J.-L. Bredas, *Mater. Horiz.*, 2014, **1**, 17–19.
- 50 Z. S. Safi, N. Wazzan and H. Aqel, *Chem. Phys. Lett.*, 2022, **791**, 139349.
- 51 M. Miar, A. Shiroudi, K. Pourshamsian, A. R. Oliaey and F. Hatamjafari, *J. Chem. Res.*, 2021, **45**, 147–158.
- 52 E. Isotta, W. Peng, A. Balodhi and A. Zevalkink, *Angew. Chem., Int. Ed. Engl.*, 2023, **62**, e202213649.
- 53 H. Zhang, N. Li, K. Li and D. Xue, *Acta Crystallogr., Sect. B*, 2007, **63**, 812–818.
- 54 K. Singh, S. Acharya and D. V. Atkare, *Ferroelectrics*, 2005, **315**, 91–110.
- 55 P. M. Woodward, *Acta Crystallogr., Sect. B*, 1997, **53**, 44–66.
- 56 W. Ye, C. Chen, Z. Wang, I.-H. Chu and S. P. Ong, *Nat. Commun.*, 2018, **9**, 3800.
- 57 Y.-H. Huang, R. I. Dass, Z.-L. Xing and J. B. Goodenough, *Science*, 2006, **312**, 254–257.
- 58 S. Choi, C. J. Kucharczyk, Y. Liang, X. Zhang, I. Takeuchi, H.-I. Ji and S. M. Haile, *Nat. Energy*, 2018, **3**, 202–210.
- 59 X. Xu, J. Zhao, M. Li, L. Zhuang, J. Zhang, S. Aruliah, F. Liang, H. Wang and Z. Zhu, *Compos. B Eng.*, 2019, **178**, 107491.
- 60 D. Liu, P. Zhou, H. Bai, H. Ai, X. Du, M. Chen, D. Liu, W. F. Ip, K. H. Lo, C. T. Kwok, S. Chen, S. Wang, G. Xing, X. Wang and H. Pan, *Small*, 2021, **17**, 2101605.
- 61 M. Irshad, Q. tul Ain, M. Zaman, M. Z. Aslam, N. Kousar, M. Asim, M. Rafique, K. Siraj, A. N. Tabish and M. Usman, *RSC Adv.*, 2022, **12**, 7009–7039.
- 62 M. Z. Kazim, M. Yaseen, S. A. Aldaghfag, M. Ishfaq, M. Nazar, Misbah, M. Zahid and R. Neffati, *J. Solid State Chem.*, 2022, **315**, 123419.
- 63 J. F. Shin, W. Xu, M. Zanella, K. Dawson, S. N. Savvin, J. B. Claridge and M. J. Rosseinsky, *Nat. Energy*, 2017, **2**, 16214.

